Effect of surfactant redistribution on the flow and stability of foam films

D. Vitasari[1,2], S. Cox[2], P. Grassia[3] and R. Rosario[3]

[1]Department of Chemical Engineering, Universitas Muhammadiyah Surakarta, Indonesia
[2]Department of Mathematics, Aberystwyth University, UK
[3]Department of Chemical and Process Engineering, University of Strathclyde, UK

The viscous froth model for 2D dissipative foam rheology is combined with Marangoni-driven surfactant redistribution on a foam film. The model is used to study the flow of a 2D foam system consisting of one bubble partially filling a constricted channel and a single spanning film connecting it to the opposite channel wall. Gradients of surface tension arising from film deformation induce tangential flow that redistributes surfactant along the film. This redistribution, and the consequent changes in film tension, inhibit the structure from undergoing a foam-destroying topological change in which the spanning film leaves the bubble behind; foam stability is thereby increased. The system's behaviour is categorised by a Gibbs-Marangoni parameter, representing the ratio between the rate of motion in tangential and normal directions. Larger values of the Gibbs-Marangoni parameter induce greater variation in surface tension, increase the rate of surfactant redistribution, and reduce the likelihood of topological changes. An intermediate regime is however identified in which the Gibbs-Marangoni parameter is large enough to create a significant gradient of surface tension but is not great enough to smooth out the flow-induced redistribution of surfactant entirely, resulting in non-monotonic variation in the bubble height, and hence in foam stability.

THE ROYAL SOCIETY
PUBLISHING

1. Introduction

The flow of an aqueous foam through a narrow channel with complex geometry is an important process. For example it occurs in medical testing of small samples of gas [1] and in the treatment of varicose veins [2]. It is also relevant in foam improved oil recovery and soil remediation [3], in which foam is injected into the porous media of an oil reservoir or contaminated soil, respectively, as the displacement fluid [4,5]. The use of foam as a displacement fluid in porous media increases the sweep efficiency and reduces the amounts of liquid and chemicals required for such a process. Despite its industrial importance, modelling such a flow is technically challenging [6], and this has prevented such flows from being fully explored.

The viscous froth model is an established method to predict the flow of a two-dimensional foam between parallel flat plates [7–9]. It is based on the balance of foam film curvatures and adjacent bubble pressures with the friction experienced by a film in a flowing foam. The model is for a dry foam (negligible liquid fraction and vanishingly small Plateau borders). The foam geometry consists of films, which meet in threes at vertices [10], and the model allows film shapes to deviate significantly from arcs of circles [11].

Previous studies using the viscous froth model have successfully described the flow of foams in microfluidic channels [1,6–8]. The model represents a system in which the foam deforms sufficiently quickly that it deviates from mechanical equilibrium. As a consequence, it can describe fast flowing foams [11]. Heretofore, the model has employed the simplifying assumption of uniform and fixed surface tension along the films, and any variation of surface tension has been neglected. Nonetheless, gradients of surface tension occur due to the elongation or contraction of the films. On a film with a gradient of surface tension, the Marangoni effect [12,13] should distribute the surfactant more evenly along the film surface [14], locally changing the surface tension and therefore affecting the deformation of the film. Viscous froth has previously been incorporated with the Marangoni effect, but only for a very simple film geometry without any enclosed bubbles [15]. Here we consider a more realistic foam geometry with an enclosed bubble such that bubble pressure must be considered. Recording bubble shape and film lengths could provide a way to validate our results experimentally using similar methods to those employed previously [1], but now varying the surface elasticity using different surfactants [16].

2. Film deformation in foam flow

When the rate of film deformation is faster than that of mechanical relaxation, a continuous deformation of the films results [17]. The stretching of a film decreases the surface concentration of surfactant, while contraction results in denser surfactant coverage on the surface. A gradient of surface concentration induces a gradient of surface tension via the Langmuir equation of state [18,19], which results in a flow of surfactant on the film surface [20] from regions with high surface tension to regions with low surface tension.

(a) Viscous froth model

Three-dimensional models of foam dynamics can be very complex and computationally expensive [7], and yet do not necessarily lead to any greater insight than a simple two-dimensional (2D) model. Hence 2D foam systems, consisting of a monolayer of bubbles between two glass plates, are often used to describe the dissipative dynamics of flowing foams [9]. Further, 2D systems are of interest in their own right, for example in well-controlled microfluidic foam flows [1,21,22].

The 2D viscous froth model is based on three physical phenomena [9]:

- the viscous drag force on a moving film resulting from friction with the confining plates,
- the pressure difference ΔP between two adjacent bubbles across a film,
- the surface tension γ acting along a curved film.

The force balance on a film with curvature C separating two bubbles b and b' is:

$$\lambda v_\perp = \Delta P_{bb'} - \gamma C_{bb'}, \tag{2.1}$$

where λ is a viscous drag coefficient and $v_\perp$ is velocity in the direction normal to the film surface.

(b) Marangoni surfactant redistribution

Our model of surfactant transport along a film surface is based on lubrication theory [14]. According to the model, the velocity on the film surface is determined by the competition between viscous shear stresses, film drainage and the Marangoni effect. In the present work, for simplicity we assume that neither film drainage nor further film thinning occur. Indeed the foam is assumed to be in the dry limit, such that the film is already very thin. In the absence of film drainage, in a film of thickness δ consisting of liquid with bulk viscosity μ, the tangential velocity $v_\parallel$ of the film surface is driven only by the Marangoni effect [13,14,23]:

$$v_\parallel = \frac{\delta}{3\mu} \frac{\partial \gamma}{\partial s}, \tag{2.2}$$

where s is position along the film.

The surface tension is in equilibrium with the surfactant surface concentration Γ, a relationship which can be expressed in terms of the Gibbs parameter G (which is assumed to be constant) using the following Langmuir equation [18]:

$$d\gamma/d\ln\Gamma \approx -G. \tag{2.3}$$

Therefore, the equation for surfactant transport (Eq. (2.2)) can also be expressed in terms of the surfactant concentration:

$$v_\parallel = -\frac{G\delta}{3\mu} \frac{\partial \ln\Gamma}{\partial s}. \tag{2.4}$$

We combine this surfactant transport equation with the viscous froth equation (Eq. (2.1)) to predict the flow of foam in a narrow channel. Hence there are two components to the movement of the films: in a direction normal to the film surface, and parallel to the tangent to the film.

These equations for the movement of points on the film do not apply to the vertices where three films meet and where the films meet the channel walls. We define separate rules to update position of these vertices in § 4(c). We will use these rules, along with Eqs. (2.1)–(2.4) above, to study the effect of surfactant redistribution on film deformation in a moving foam. In order to do so, we consider different channel geometries to highlight different aspects of the system.

3. Geometry of the system

We analyse a two-dimensional "lens" structure [7] flowing through a narrow channel. The structure consists of a bubble attached to one wall of the channel and connected to the other side of the channel by a single film. The structure is simple, yet it represents the components of a foam: films acted on by distinct pressures, a three-fold vertex where films meet, known as a Plateau border, and vertices where the films meet the walls. Previous work has shown the rich dynamical response of the lens structure when a driving force is applied [7].

We consider three different channel geometries:

  (i) a straight channel with flat walls on both sides of the channel (Fig. 1), which allows us to establish steady state foam geometries for different driving conditions and material parameters such as the Gibbs elasticity.
  (ii) a channel with an abrupt decrease in width, but which is otherwise straight, which allows us to probe the relaxation back to steady state flow after a change in channel geometry.
  (iii) a channel with a periodically-varying sinusoidal shape, in which the channel geometry varies continuously as the lens flows through it.
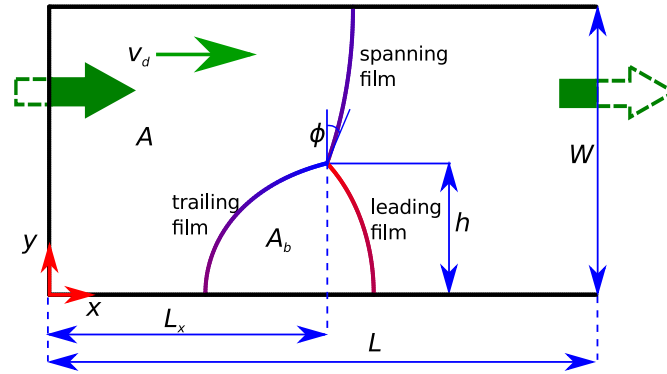
Figure 1: Geometry of the straight channel, with channel width W. The bubble area is A_b, h is the height of the vertex at the top of the bubble, v_d is the applied driving velocity, L is the length of one period of the channel and L_x is the horizontal distance travelled by the vertex. The different parts of the foam are labelled: the leading and trailing films on the bubble, and the spanning film, making an angle ϕ at the vertex, connecting it to the other channel wall. The area to the left of the lens bubble and spanning film forms a further bubble with area A; this bubble is inflated to push the lens along the channel.
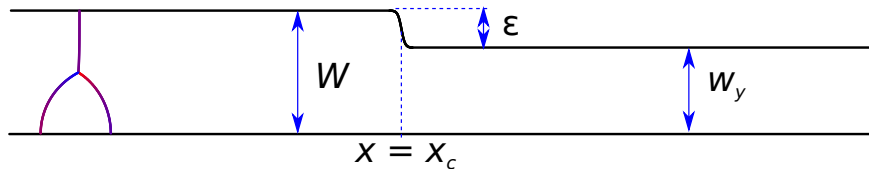

Figure 2: The geometry of the channel with an abrupt change in width of size ε at horizontal position $x = x_c$.

We create a geometry with periodicity in the flow direction for the first and the third cases, so that situations in which long-time relaxation to a periodic state with transients eliminated can be simulated. Thus the lens structure passes through each channel geometry repeatedly: when it leaves the channel at the downstream end it re-appears upstream.

A periodic boundary condition is not required for the channel with an abrupt change in width, as the relaxation can be observed using a single long channel with a length determined by our simulations in the previous geometry. Specifically, we consider a constricted region of depth ε initiated at horizontal position $x = x_c$ (see Fig. 2). The transition in channel width from wide to narrow is determined by a parameter β, giving the width profile:

$$w_y(x) = W - \frac{\varepsilon}{2} \left\{ 1 + \tanh \left[\frac{x - x_c}{\beta} \right] \right\}. \tag{3.1}$$

In our simulations we take $\beta = 0.03W$, $10W \leq x_c \leq 30W$ (which is sufficient for the lens to relax to steady state before reaching the constriction) and find that, for the driving velocities considered, a constricted channel length of $10W$ after $x = x_c$ is sufficient for the lens structure either to relax to steady state in the constricted part of the channel or else to break up. Once either of those events occurs, depending on the applied driving velocity, the simulation is stopped.

The third channel geometry has a constriction in which one wall is sinusoidal, as shown in Fig. 3. This shape provides a gradual change of channel width and a sinusoid is selected to maintain the periodicity of the channel geometry. The depth of the constriction is ε and, with
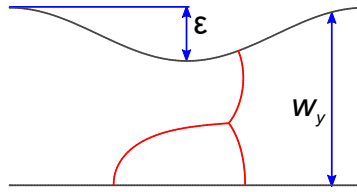
Figure 3: Illustration of the lens structure in a sinusoidally-constricted channel with depth profile $w_y(x)$ given in Eq. (3.2).

one period of the channel length denoted by L, we use the equation

$$w_y(x) = W - \frac{\varepsilon}{2}\left(1 - \cos\left(\frac{2\pi x}{L}\right)\right). \tag{3.2}$$

In our simulations we set the length of one period to be twice the channel width ($L = 2W$).

4. Numerical simulation

The equations of motion must be solved numerically, so in § 4(a) we first use dimensional analysis to simplify them. This indicates that a key parameter is the ratio of velocities of the tangential and the normal motions, namely the Gibbs-Marangoni parameter, which is presented in Eq. (4.4). We explain the discretisation used in the numerical implementation of the model in § 4(b) and how this adapts to accommodate the motion tangential to the film, Eq. (4.9), due to surfactant redistribution. In § 4(c) we explain how we treat vertices where three films meet and where the film meets the wall. Our pressure calculation is described in § 4(d).

(a) Dimensional analysis

The computations were carried out with the governing equations in dimensionless form. The unconstricted width of the channel W is used as the relevant length scale, surfactant concentrations are taken relative to the equilibrium value Γ_{eq}, which is related to the equilibrium surface tension γ_{eq}. We use a superscript asterisk to denote dimensionless variables.

The dimensionless viscous froth equation, from Eq. (2.1), is

$$v_\perp^* = \Delta P^* - \gamma^* C^*, \tag{4.1}$$

where $v_\perp^* = v_\perp W\lambda/\gamma_{eq}$ is the dimensionless velocity in the direction normal to the film surface, $P^* = PW/\gamma_{eq}$ is the dimensionless bubble pressure, $\gamma^* = \gamma/\gamma_{eq}$ is the dimensionless surface tension and $C^* = CW$ is the dimensionless film curvature. Similarly, the Marangoni equation (2.4) for surfactant transport becomes:

$$v_\parallel^* = -\frac{1}{3}\frac{\partial \ln \Gamma^*}{\partial s^*}, \tag{4.2}$$

where $v_\parallel^* = v_\parallel \mu W/(G\delta)$ is the dimensionless tangential velocity, $\Gamma^* = \Gamma/\Gamma_{eq}$ is the dimensionless surfactant surface concentration and $s^* = s/W$ is the dimensionless position along the film.

These two equations have different time scales. For the viscous froth model the dimensionless time scale is $t_V^* = t\gamma_{eq}/(W^2\lambda)$ and for the Marangoni equation the dimensionless time scale is $t_M^* = tG\delta/(W^2\mu)$. The time scales are related by

$$t_M^* = \frac{G\delta\lambda}{\gamma_{eq}\mu}t_V^*. \tag{4.3}$$

The prefactor in Eq. (4.3) is defined as the Gibbs-Marangoni parameter:

$$G_M = G\delta\lambda/(\gamma_{eq}\mu). \tag{4.4}$$

If $G_M \gg 1$ the tangential movement (that endeavours to keep the surface tension uniform) is fast compared with the normal motion. On the other hand, when $G_M \ll 1$, the tangential movement is slower than the normal motion. To simplify the notation, from this point on, the dimensionless variables will be presented without asterisks.

The relation between the driving velocity imposed to move the foam structure and the characteristic velocity associated with the surfactant equilibration mechanism is therefore important in determining the system behaviour. The relationship, similar to other viscoelastic systems, can be described using the Deborah number De [24,25], expressed as the ratio of the driving velocity (non-dimensionalised in the same fashion as $v_\perp$) to the Gibbs-Marangoni parameter:

$$De = \frac{v_d}{G_M} = \frac{\gamma_{eq}\mu}{G\delta\lambda}v_d.$$
(4.5)

The Deborah number distinguishes the time required for tangential Marangoni surfactant redistribution from the time required to deform a film due to the flow. It therefore represents the effect of the selected Gibbs parameters on surfactant transport on the film surface when various driving velocities are applied. Eq. (4.5) relates the Deborah number to the dimensionless Gibbs parameter G/γ_{eq} and the dimensionless driving velocity, as follows:

$$\frac{G}{\gamma_{eq}}De = \frac{\mu}{\delta\lambda}v_d.$$
(4.6)

In our simulations the value of $\mu/(\delta\lambda)$ is fixed at 0.02, therefore the Deborah number De is a linear function of the driving velocity v_d.

(b) Movement of points on films

A lens bubble with fixed area A_b is pushed along the channel with driving velocity v_d. To do so, an additional bubble which fills the whole channel width is placed upstream. The area A of this bubble increases at a fixed rate while one end is kept fixed at $x = 0$, as denoted by the straight line on the left hand side of Fig. 1.

The computations were carried out using Surface Evolver [26,27] which, although we do not primarily use it to minimise the surface energy of bubbles, offers tools for ensuring that the tessellation of the films is well-controlled and for probing their properties, such as curvature. The dimensionless maximum channel width is set at $W = 1$. An equilibrium structure was first obtained using the built-in Surface Evolver length minimisation method. In this step, the films are divided into short equal length segments with dimensionless lengths in the range $0.004 - 0.012$, and the surfactant is distributed evenly along the films, resulting in uniform surface tension throughout the structure.

Once the equilibrium structure is obtained, the surface length minimisation method is turned off and the area of the driving bubble is increased at a fixed rate. The viscous froth equation, Eq. (4.1), is applied to each point between segments to move it in the direction normal to the film surface. The curvature C at any point between two segments is determined using the difference in the direction of the surface tension force acting on adjacent segments, normalised by their average length. The dimensionless viscous froth time step is set at $\Delta t_V = 5 \times 10^{-6}$, from which the Marangoni time step can then be calculated as $\Delta t_M = G_M \Delta t_V$.

Films deform as they move, according to the viscous froth model. As a result, segments will stretch or shrink. The number of surfactant molecules on each segment is conserved, so changing the length of each segment will change the concentration of surfactant upon it and hence its surface tension. We write the concentration of surfactant on a segment i at any given time j as $\Gamma_{(i,j)}$ and the segment length as $s_{(i,j)}$. The update rule for surfactant concentration depends on its value at the previous time step and the old and new segment lengths according to

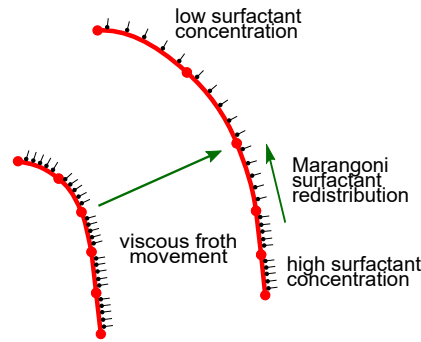$$\Gamma_{(i,j)} = \Gamma_{(i,j-1)}s_{(i,j-1)}/s_{(i,j)}.$$
(4.7)

Figure 4: A schematic showing the movement of the points on film segments due to the viscous froth movement in the normal direction and the Marangoni surfactant redistribution of points towards lower surfactant concentrations in the tangential direction.

After the new value of Γ is calculated, the surface tension on each segment is calculated using the Langmuir equilibrium:

$$\gamma_{(i,j)} = 1 - \frac{G}{\gamma_{eq}} \ln \Gamma_{(i,j)}. \tag{4.8}$$

The Marangoni effect arising from gradients of surface tension redistributes surfactant along the film. We use Eq. (4.2) to update the positions $\underline{x}$ of the points by moving them in the direction of the tangent $\underline{t}_\parallel$ according to:

$$\underline{x}_{(i,j)} = \underline{x}_{(i,j-1)} - \frac{\Delta t_M}{3} \frac{\ln \Gamma_{(i,j)} - \ln \Gamma_{(i-1,j)}}{(s_{(i,j)} + s_{(i-1,j)})/2} \underline{t}_\parallel. \tag{4.9}$$

Fig. 4 shows how points move in a direction normal to the film and how the Marangoni effect moves points tangentially from regions with high surface concentration to regions with lower surface concentration. The concentration of surfactant and the surface tension on each segment are updated via Eqs. (4.7)–(4.8) after every change of segment length. The numerical method is most reliable when it deals with segments with similar lengths so any segment with length less than 0.004 is merged with an adjacent segment and the amount of surfactant contained in the two segments is added. Conversely, if a segment has length greater than 0.012 it is divided into two shorter segments and the surfactant distributed equally between the new segments.

In addition, an "averaging" operation is applied at each time step to return the tessellation to a more uniform one. The idea, which is already implemented in Surface Evolver as the "V" command [26], is to move a point towards the mean position of points at the other ends of the adjacent segments, while preserving the film curvature. The operation narrows the distribution of segment lengths along a film, thereby reducing the need to delete segments with length below the minimum threshold. For the case with the Marangoni surfactant redistribution ($G_M \neq 0$), after the "averaging" operation, the amount of surfactant carried by the segment on each side of the point needs to be rebalanced, as explained in [14]. Without any Marangoni surfactant redistribution, such that $G_M = 0$ (or more specifically if $G/\gamma_{eq} = 0$), there is no need to consider reassignment of surfactant concentration as this has no bearing on the dynamics of the system.

(c) Movement of vertices

The viscous froth and the Marangoni equations apply only to points along the films. At vertices where three films meet and/or films meet the channel wall, a separate approach is taken.

In this context, the Fermat-Torricelli problem [28] is to minimise the sum of distances of a three-fold vertex from three neighbouring points with weights given by the surface tensions. The algorithm given in [28] is used to determine the position of the vertex based on the positions

of the three neighbouring points on the three discretised films. The surfactant is assumed to be tied to each film, and we prohibit transfer of surfactant between films at the vertex.

Where a film meets a channel wall, the wetting layer on the wall is assumed to apply an equal surface tension force in each direction. In consequence, the film will be perpendicular to the wall. The position of the vertex where the film meets the wall is therefore adjusted, so that the segment joining that vertex to the nearest adjacent point on the same film coincides with the normal to the channel wall.

(d) Calculation of bubble pressures

The pressure within each bubble is calculated based on the principle that any change in the bubble pressure and/or film curvature could tend to change the bubble area. The change of area A of a bubble is equal to the integral of the normal velocity $v_\perp$ around it; therefore using the equation of motion, Eq. (4.1), the change of bubble area can be calculated as [9]:

$$\lambda \frac{\mathrm{d}A}{\mathrm{d}t} = \lambda \oint_{\partial b} v_\perp \mathrm{d}l = \oint_{\partial b} (\Delta P - \gamma C) \mathrm{d}s, \tag{4.10}$$

where the expression $\mathrm{d}s$ represents an element of film length. We think of these integrals as a sum over the discretised segments making up the films, so rearranging and integrating Eq. (4.10) around a bubble b results in

$$\lambda \frac{\mathrm{d}A_b}{\mathrm{d}t} + \sum_{\text{segments } i} \gamma_i C_i s_i = \sum_{\text{bubbles } b'} (P_b - P_{b'}) s_{bb'}, \tag{4.11}$$

where the subscript b' denotes each of the neighbouring bubbles and therefore $s_{bb'}$ represents the length of a segment of film separating two bubbles. Since bubble areas are either conserved or inflated at a known rate, for a foam of n bubbles there will be n equations, leading to a matrix system for the vector of pressures, P_b:

$$\mathcal{C}_b = \mathcal{L}_{bb'} P_{b'}, \tag{4.12}$$

where $\mathcal{C}_b$ denotes a vector in which each term is obtained from the left-hand side of Eq. (4.11), consisting of the product of tensions and curvatures summed over segments around each bubble, plus rates at which bubble areas are inflated if relevant. The vector $\mathcal{C}_b$ may include a contribution from inflating or deflating the area of the lens bubble back towards its target area as a means of correcting any truncation error that may otherwise cause its area to drift. The term $\mathcal{L}_{bb'}$ is the matrix in which the $(b, b')^{\text{th}}$ entry is the length of the film separating bubble b from bubble b'. We use Surface Evolver's in-built matrix manipulation routines to solve Eq. (4.12).

5. Simulation results

A particular driving velocity (referred to the unconstricted part of the channel) $v_d = (\mathrm{d}A/\mathrm{d}t)/W$ is applied to move the lens, resulting in film deformation and changes to the vertical height h and the horizontal position L_x of the three-fold vertex, as indicated in Fig. 1. At low velocity, the lens structure is stable and the spanning film remains attached to the bubble. For sufficiently fast flow, the structure breaks up: the spanning film runs ahead, and detaches from the bubble leaving it behind [6,7]. The deformation of the films and subsequent breakdown is illustrated in Fig. 5. Note that both the trailing film and (at least in a straight channel) the spanning film stretch due to the motion while the leading film shrinks. We now examine the effect of surfactant redistribution on film deformation and on the critical velocity above which foam breakdown occurs. The dimensionless parameters are summarised in Tab. 1.

Note that the viscous drag coefficient is rescaled here as the dimensionless parameter $\delta\lambda/\mu$ (see Eq. (4.6)). The drag coefficient λ is particularly difficult to estimate [1,7,29], with different authors using different units and suggesting different dependencies on parameters such as channel height and capillary number. For simplicity, particularly in the calculation of the pressure within
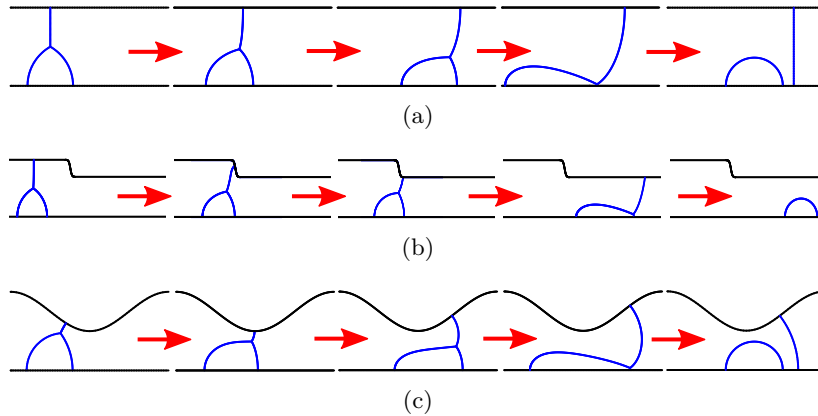
Figure 5: Each sequence of images illustrates how the lens structure is progressively deformed, starting from rest, as it moves along a channel at constant velocity. In each case, the velocity is sufficiently large that significant film deformation occurs and the structure eventually breaks down. (a) Straight channel. (b) Channel with abrupt change in width. (c) Sinusoidally-constricted channel.

Table 1: The dimensionless parameters of the simulations (at equilibrium: lens bubble area $A_b = 0.074W^2$ corresponds to spanning film length $l_s = 0.769W$, whereas $A_b = 0.205W^2$ corresponds to spanning film length $l_s = 0.501W$)

Variable	Symbol	Value
Lens bubble area	A_b	$0.074W^2 - 0.205W^2$
Driving velocity	v_d	$1 - 7$
Gibbs parameter	G/γ_{eq}	$0 - 0.125$
Gibbs-Marangoni parameter	$G_M = G\delta\lambda/(\mu\gamma_{eq})$	$0 - 6.25$
Ratio of viscous drag coefficients	$\delta\lambda/\mu$	50

the bubbles, we assume a linear drag law in the viscous froth equation [9] and take values of drag coefficient $\lambda = 290 \, \mathrm{kg \, m^{-2} \, s^{-1}}$ and liquid viscosity $\mu = 1.16 \times 10^{-3} \, \mathrm{Pa \, s}$ from one particular experimental study [29]. To illustrate the model, for the present study we selected $\delta\lambda/\mu = 50$ suggesting $\delta \approx 2 \times 10^{-4} \, \mathrm{m}$, which might correspond to a very thick foam film around the time a foam is first formed, before film drainage has occurred.

In the following we examine the maximum velocity for which the structure of the lens is stable for each set of parameters (bubble area A_b, constriction depth ε and Gibbs-Marangoni parameter G_M). First, in § 5(a) we study the straight channel to determine the effect of these parameters on the distribution of surface tension and on the film deformation within a uniform width channel. In § 5(b) we consider flow along the channel with an abrupt change in width to evaluate how the sudden increase in the effective driving velocity affects the relaxation and stability of the foam structure. Then in § 5(c) we consider stability in the sinusoidally-varying channel. In each case, above a critical velocity, the spanning film will leave the bubble behind.

(a) Straight channel

As the lens moves along a straight channel, viscous friction causes its shape to change. The amount of friction depends upon the length of the film normal to the direction of motion [9,30], while the pressure in the bubble(s) causes films to move normal to the local inclination of the
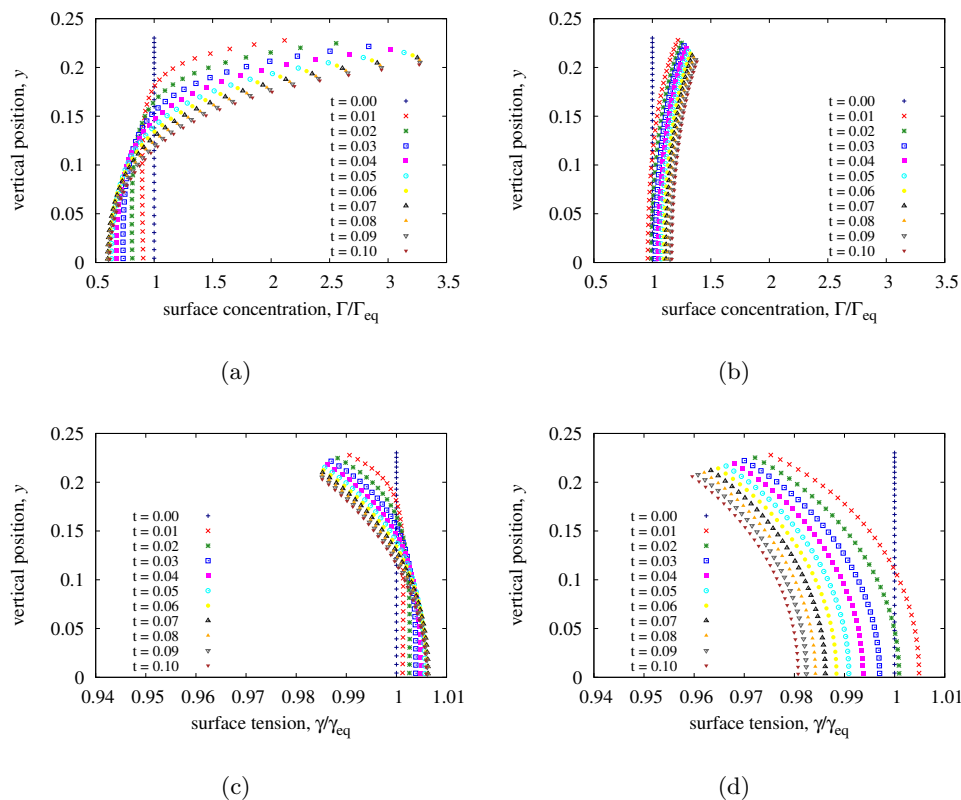
Figure 6: The distribution of surfactant concentration at different positions on the leading film in a straight channel at early times simulated (a) using $G/\gamma_{eq} = 0.0125$, $G_M = 0.625$ and (b) using $G/\gamma_{eq} = 0.125$, $G_M = 6.250$. This is compared with the corresponding distribution of surface tension: (c) same parameters as (a); (d) same parameters as (b). The distance between the points corresponds to the length of each segment. Other parameters are lens bubble area $A_b = 0.074$ and driving velocity $v_d = 5$.

interface. The channel with constant width allows us to explore various distributions of surfactant by varying the Gibbs parameter G/γ_{eq} while keeping other parameters fixed. At $G/\gamma_{eq} = 0$ the surfactant will not be redistributed by tangential motion along the film surface since, according to the Langmuir equilibrium in Eq. (4.8), the surface tension is constant and uniform in this case. Surfactant concentration is non-uniform of course in the $G/\gamma_{eq} = 0$ case, since even purely normal motion on curved films is sufficient to stretch or shrink film elements [7].

Fig. 6 shows values of surface tensions and surfactant surface concentrations on the segments of the leading film at very early times, when the motion first starts, for two different values of the Gibbs-Marangoni parameter, $G_M = 0.625$ and $G_M = 6.25$. The surfactant is less evenly distributed when G_M is small, resulting in a large variation of surfactant concentration along the film (Fig. 6a). Since small G_M is associated with a small value of the Gibbs elasticity, the large range of surfactant concentration does not lead to a particularly broad distribution of surface tension (Fig. 6c). On the contrary, when the value of G_M is large, the surfactant is more evenly distributed along the film, resulting in a narrower range of surfactant concentration (Fig. 6b), but since the value of the Gibbs elasticity is large, the Langmuir equation (Eq. (4.8)) implies a broad range of values of surface tension (Fig. 6d).

Fig. 7 shows the distribution of surface tension on the trailing and spanning films with large Gibbs-Marangoni parameter G_M again at very early time. A high value of the driving velocity
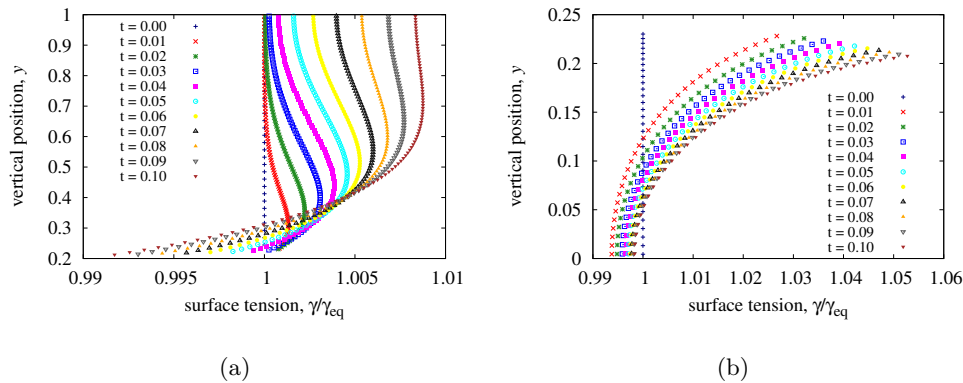
Figure 7: Distribution of surface tension at early times (a) on the spanning film and (b) on the trailing film. Parameters as in Fig. 6b.

v_d is again chosen, to emphasise how the distribution of surface tension changes as the films deform. In contrast to the profile of surface tension on the leading film in Fig. 6d, where the range of variation of surface tension decreases over time, the surface tension on the spanning and trailing films has a wider variation with increasing time, which we rationalize as follows.

The lens bubble is enclosed by *two* films (the leading and trailing films) moving downstream, and therefore experiences a greater effective drag (per unit height) than the spanning film. To accommodate this difference, while remaining attached to the bubble, the spanning film becomes curved. In fact, it responds (at least far from the vertex at the top of the bubble) in a similar manner to an interface under so called "pressure-driven growth" flow [31,32]: the points connecting segments move downwards as the film slides along the channel, carrying surfactant with them. Hence the surfactant on the spanning film will accumulate near the vertex, increasing the surfactant concentration in this region, and consequently lowering the surface tension in comparison with the other end of the spanning film (Fig. 7a).

A similar argument applies to the leading film of the bubble, although the orientation of the film, at least initially, is driven more by the pressure inside the lens bubble than any differences in viscous drag. Surfactant is again carried toward the vertex, so the tension of this film becomes lower close to the vertex at the top of the bubble compared to near the channel wall. As the system continues to evolve, in contrast to the uneven stretching rate of the segments on the spanning film, those on the leading film experience relatively uniform drag during the film movement as the structure deforms, since they become mostly inclined in the direction normal to the film movement (see Fig. 5), resulting in a narrower range of shrinking rate of the segments compared to the other two films. The Marangoni surfactant redistribution is then able to limit the variation of surface tension on the leading film, bringing about a reduction in the gradient of surface tension over time, particularly when the Gibbs elasticity is large (Fig. 6d).

On the trailing film, greater drag is experienced by segments near the wall where they are inclined perpendicular to the direction of the overall motion. Moving up towards the vertex, the trailing film aligns more with the direction of overall motion, implying less normal motion and thereby less drag. The smaller drag experienced by the segments near the vertex on the trailing film results in them running ahead of points lower down, depleting the surfactant near the vertex, and resulting in higher surface tension there (Fig. 7b).

When the driving velocity is large, the Marangoni surfactant redistribution may not be fast enough to eliminate any gradient of surfactant concentration. As a result, large gradients of surfactant concentration can be sustained (Fig. 6a). The balance of the driving velocity and the Marangoni surfactant redistribution is represented by the Deborah number *De* in Eq. (4.5). The Marangoni surfactant redistribution becomes dominant, reducing the gradient of surface
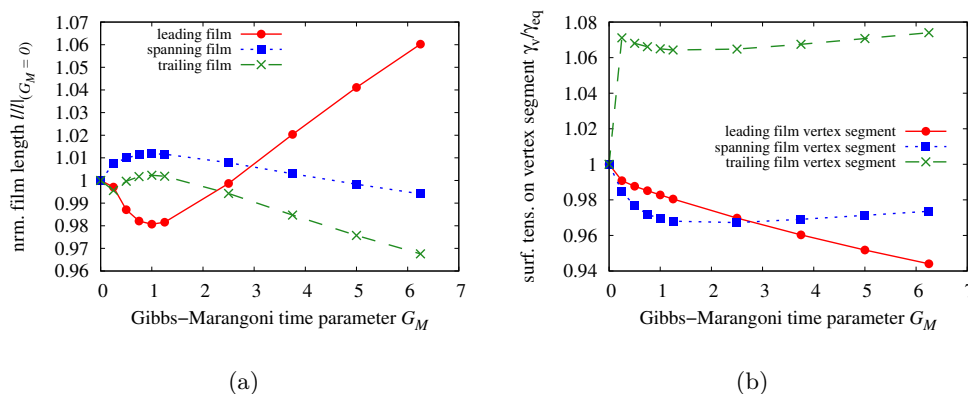
Figure 8: (a) The length of each film when the lens structure is moving steadily (for long times) along a straight channel. The length is shown normalized by its length for $G_M = 0$. (b) The corresponding surface tensions of the segment on each film that is adjacent to the three-fold vertex. The simulation parameters are $A_b = 0.074$ and driving velocity $v_d = 5$.

concentration along a film, when the Deborah number is small, or equivalently when the driving velocity is small. The movement of the points due to the Marangoni surfactant redistribution also reduces the rate of stretching and shrinking of the segments, increasing foam stability. According to Eq. (4.5), in the limit of large G_M, the rate for surfactant to be re-equilibrated should eventually dominate the deformation rate associated with the driving velocity, and the system should approach the limit of uniform surfactant concentration. At low G_M the film segments stretch or shrink more, and gradients of surface concentration along the film are sustained. Gradients of surface tension however depend on gradients of surfactant concentration multiplied by G/γ_{eq} (see Eq. (4.8)), and this is analogous to multiplying by G_M since $\mu/(\delta\lambda)$ is fixed here. Thus larger G_M gives a narrower distribution of surfactant concentration but a wider distribution of surface tension (Figs. 6d, 7a and 7b).

In between these limiting cases of $G_M = 0$ and large G_M, our simulations identify an intermediate region in which there is significant surfactant redistribution along the trailing film. This situation persists even in much later times when the configuration has attained a steady state ($t \gg 1$). For small but finite G_M, Fig. 8b shows the trailing film being strongly stretched near the vertex, and hence acquiring a large local surface tension there, but with only modest changes in surface tension near the vertex for the other two films. Moreover the nature of Eq. (4.8) is such that surfactant depletion has more impact on surface tension than surfactant accumulation. The imbalance in the surface tensions at the vertex causes it to move downwards (according to the Fermat-Torricelli rule), shortening the leading film and lengthening the spanning film (Fig. 8a). As G_M increases however, we see a significant reduction in the surface tension in the leading film at the vertex (Fig. 8b again). This leads to less downward and forward pull on the vertex, making it now migrate backwards and upwards. The leading film then lengthens, at the expense of the trailing and spanning films (Fig. 8a).

The vertex position corresponds to the height h of the bubble. The effect of the Gibbs-Marangoni parameter on the steady state height of the bubble h_{ss} at various driving velocities is shown in Fig. 9. For a given driving velocity the height decreases at small G_M, as per the length of the leading film, and then as G_M increases further, the bubble "rebounds" and increases in height. This effect is greater at higher velocities, where the film deformation is greater for a given G_M (i.e. when De is greater), resulting in a larger gradient of surface tension along the film and a greater imbalance of surface tension on the segments surrounding the vertex. The intermediate regime can be considered to finish around the point at which the Marangoni
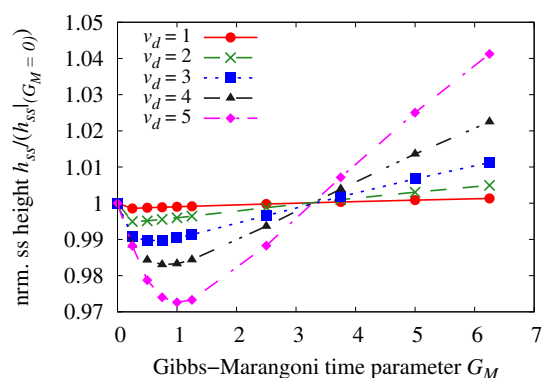
Figure 9: The effect of Gibbs-Marangoni parameter G_M on the steady state vertex height h_{ss} at various driving velocities. The height is normalised by the height of the case without the Marangoni effect ($G_M = 0$) to allow comparison between different driving velocities. The area of the lens is $A_b = 0.074$ in all these simulations.

surfactant redistribution starts to overcome structural changes induced by the driving velocity, which occurs at around $G_M = 3$, where the response, at least for h_{ss} and film lengths, is as if the tensions were again uniform.

(b) Abrupt change in channel width

To see the effect of an abrupt change in the channel width, the lens structure was driven along the second channel geometry at a set velocity for different values of G_M. Fig. 10 shows how the vertex height first reaches a steady state in the wide part of the channel for the case $v_d = 2$. The height depends on G_M, as explained above, with the shortest bubble being found for an intermediate value of G_M.

As the bubble passes the constriction there is an immediate drop in the vertex height, before it rebounds to a new steady state, lower than before. Surprisingly, in the new steady state the shortest bubble is found for the highest value of G_M (Fig. 10b). Note also the weaker relaxation at high G_M: when the channel width drops suddenly, the bubble area is conserved and so the length of the spanning film must decrease. Consequently its surface tension also reduces and the vertex is pulled downwards by the other two films. After that the system relaxes again, and surfactant is re-distributed along the spanning film at a rate determined by G_M, while tensions are controlled by the Gibbs elasticity G. Here, it appears that the latter dominates in determining the subsequent evolution.

The spanning film undergoes a significant change in surfactant surface concentration at the point where the channel is constricted. At high G_M the increase of surfactant surface concentration on the spanning film results in a large decrease in surface tensions, preventing the spanning film from pulling up the vertex, thereby keeping the vertex height small. On the other hand, at low G_M the surface tensions on the spanning film do not change much despite there being a change in the surfactant surface concentrations. This helps to pull the vertex up.

Figure 9 shows that as the films approach the constriction, the height of the vertex h/W rises, then dips, then rises again with relaxation towards a final steady state. Although we will not give full details here, we assert that this upward-downward-upward motion is driven by significant pressure changes in the bubbles as the constriction is approached. These pressure changes drive film motion, which therefore induces vertex motion. What drives the underlying pressure changes near the constriction is the need for the top of the spanning film to reorient suddenly as the upper wall of the channel reorients from horizontal to downward sloping and
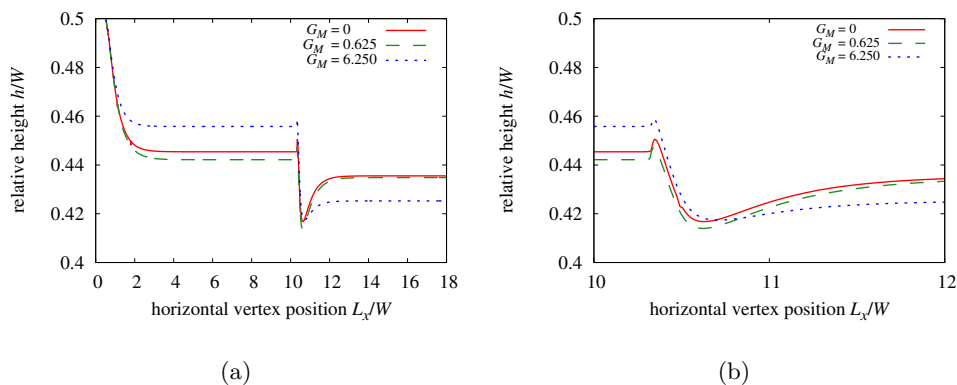
Figure 10: (a) Bubble height for a lens structure passing through an abrupt constriction for three values of the Gibbs-Marangoni parameter G_M. (b) Zoom on (a) close to where the channel width changes abruptly. Simulation parameters are $\varepsilon = 0.3$, $x_c = 10$, lens bubble area $A_b = 0.205$, driving velocity $v_d = 2$.
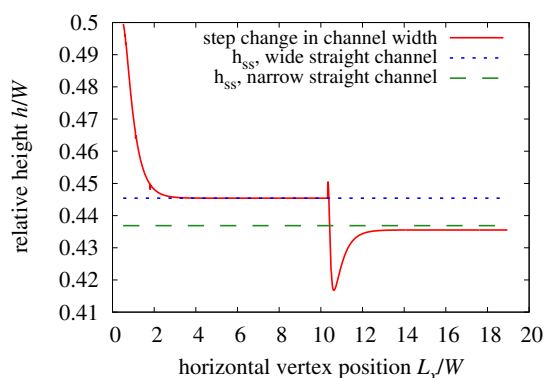

Figure 11: Vertex height in a channel with an abrupt change in width compared with the steady-state vertical position h_{ss} of the vertex in a straight channel of width equal to the wide or narrow part. Simulation parameters are lens bubble area $A_b = 0.205$ and driving velocity $v_d = 2$, constriction size $\varepsilon = 0.3$, $x_c = 10$ and Gibbs-Marangoni parameter $G_M = 0$ (no Marangoni effect).

back to horizontal as illustrated in Fig. 5b. This requires high curvatures near the top of the spanning film, influencing the curvature term on the left hand side of Eq. (4.11). Moreover, at the constriction, the length of the spanning film rapidly decreases, and this affects the $s_{bb'}$ term on the right hand side of Eq. (4.11), and hence affects the pressures.

The steady-state height of the vertex in the channel with an abrupt change of width can be predicted using data obtained from the simulation in a straight channel as presented in Fig. 11. To calculate the steady-state height, maintaining the bubble area while narrowing the channel width is equivalent to having a larger bubble area within a fixed channel width. However, near the constriction, the dynamics are more complicated due to the change of pressure as the spanning film reorients, as discussed previously.

At faster driving velocity, the structure may become unstable either when passing into the constriction, or when seeking a new steady state in the constricted channel. With a driving velocity of $v_d = 4$, Fig. 12 shows that with a moderate value of $G_M = 0.625$ the lens is not stable
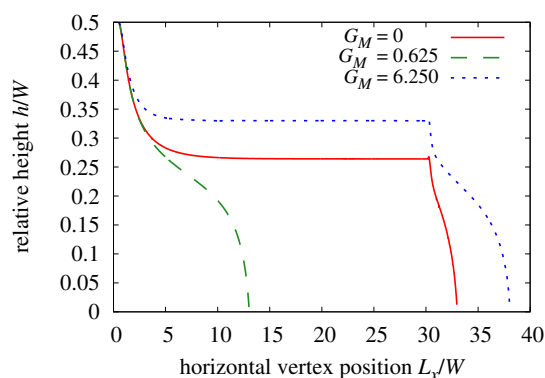
Figure 12: Instabilities of the foam structure at high velocity in a channel with an abrupt change in width. At $G_M = 0.625$ the lens is unstable in the wide part of the channel upstream, while for the other values of G_M ($G_M = 0$ and $G_M = 6.250$) the instability occurs when the lens moves into the constricted region. Simulation parameters are $\varepsilon = 0.3$, $x_c = 30$, lens bubble area $A_b = 0.205$, driving velocity $v_d = 4$.

in the wide part the channel, while for $G_M = 0$ and $G_M = 6.250$ it is stable there but *not* in the narrower part of the channel, where it moves more quickly but with a shorter spanning film. As noted in § 5(a), the vertex is lower for intermediate values of G_M, which makes the lens less stable in that regime, particularly at high driving velocity. The instability occurs when the vertex touches the channel wall ($h = 0$), then the spanning film detaches and leaves the bubble behind. Previously, we found that the larger the bubble relative to the channel width, the lower the driving velocity required to trigger instability [6,7]. The velocity $v_d = 4$ in Fig. 12 is selected [6] such that for the chosen bubble area $A_b = 0.205$ and constriction size $\varepsilon = 0.3$, in the case without surfactant redistribution ($G_M = 0$), the lens structure will be stable in the wide part of the channel but unstable in the narrow part.

(c) Flow in a sinusoidally-constricted channel

In the channel with a continuously-varying width, there is a continuous deformation of the films while the structure is moving. As a consequence, the Gibbs-Marangoni parameter determines the extent to which the corresponding film deformation can be accommodated: surfactant redistribution is key to retaining stability of the foam structure.

As a benchmark, a simulation in a sinusoidally-constricted channel (Fig. 3) was carried out for $G_M = 0$ (no Marangoni effect). The evolution of the height of the vertex in this case is compared to the steady-state height of the vertex for a lens in a straight channel of width equal to the maximum or minimum width of the sinusoidally-constricted channel in Fig. 13. Despite channel width changing in a more gradual manner compared to the case of an abrupt constriction, a large variation in vertex height occurs, exceeding the bounds expected from the straight channel case, presumably due to the small wavelength of the sinusoidal constriction in this example.

We now include surfactant redistribution (Fig. 5c) and, with specified channel and bubble geometry, vary the driving velocity and record the height of the vertex in Fig. 14. Three values of G_M are considered, identically zero, small ($G_M = 0.625$) and large ($G_M = 6.25$). Allowing significant surfactant redistribution is expected to result in a more stable structure.

In the case of low driving velocity ($v_d = 2$) in Fig. 14a, it appears that at larger G_M the leading film is less deformed, as demonstrated by the taller bubble. At high velocity (Fig. 14c), the spanning film leaves the bubble behind for all values of G_M considered, although this occurs further along the channel as G_M increases. At intermediate driving velocity (Fig. 14b), the
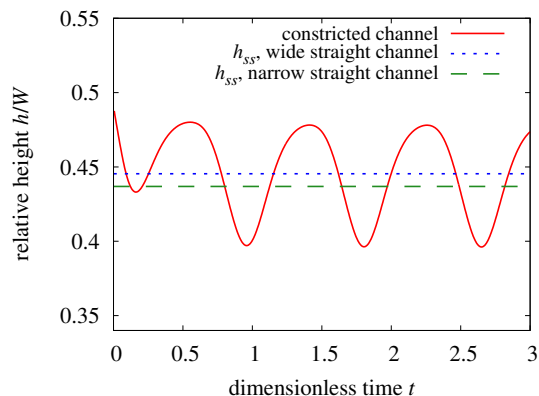
Figure 13: Vertex height in a sinusoidally-constricted channel with $\varepsilon = 0.3$ compared to the steady-state vertex heights in straight channels of width 1.0 and 0.7. Simulation parameters are lens bubble area $A_b = 0.205$, driving velocity $v_d = 2$, and Gibbs-Marangoni parameter $G_M = 0$.
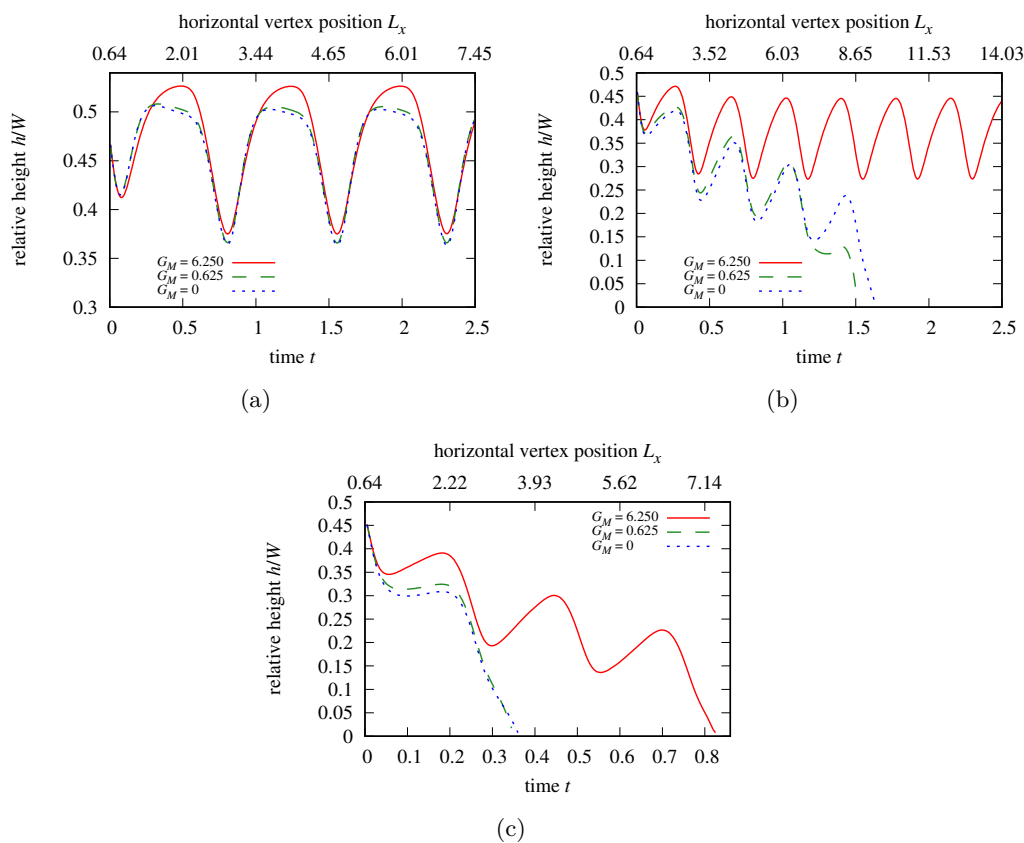

(a)

(b)

(c)

Figure 14: Change in the vertex height as the lens moves along a channel with varying width for three values of G_M. Each graph shows a different driving velocity: (a) $v_d = 2$, (b) $v_d = 4$, (c) $v_d = 6$. Simulation parameters: $\varepsilon = 0.5$, lens bubble area $A_b = 0.205$.
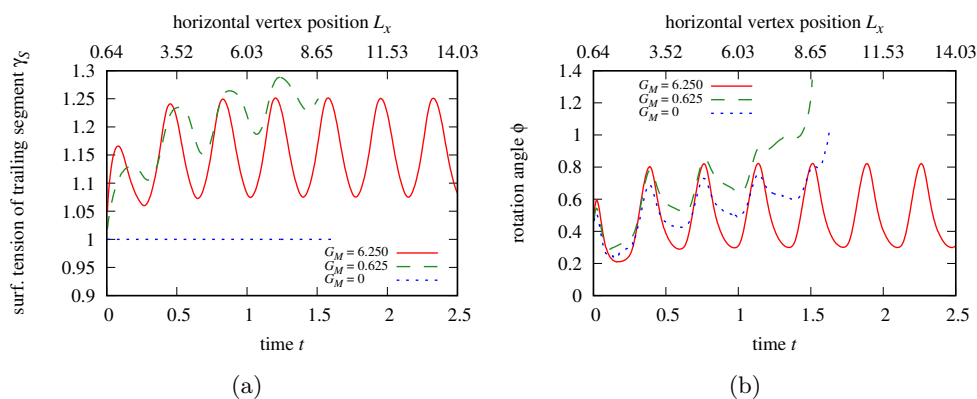
Figure 15: (a) Surface tension on the segment adjacent to the vertex on the trailing film over time for different G_M in a sinusoidally-varying channel. (b) Rotation angle of the spanning film over time. Simulation parameters: $\varepsilon = 0.5$, lens bubble area $A_b = 0.205$, driving velocity $v_d = 4$.

spanning film leaves the bubble behind only for small G_M or G_M identically zero, but with the bubble being left behind sooner for small non-zero G_M. With low Gibbs-Marangoni parameter, the redistribution of surfactant on the film is very slow. Although there is only a small range of surface tension values along most of the film lengths, there is nonetheless a significant difference of surface tensions among the segments adjacent to the vertex. As a consequence the vertex will move, according to the Fermat-Torricelli rule, in such a way as to increase the rotation angle ϕ relative to the vertical (see Fig. 1) of the spanning film, which reduces the length of the leading film [24]. However the Marangoni surfactant redistribution, in particular for large Gibbs elasticity, counteracts the shrinking of the leading film, as in film relaxation following a T1 process [33,34], resulting in a more stable structure.

Fig. 15a shows the evolution of the surface tension on the segment of the trailing film adjacent to the vertex with a driving velocity of $v_d = 4$. As the structure moves, the film stretches and contracts. However, the stretch is mainly accommodated by the segments close to the vertex. In consequence, at low G_M the surface tension in that region keeps increasing, deviating further from the surface tension of the segments adjacent to the vertex on the other two films. Since G_M is low, the rate of surfactant transport is not sufficient to compensate this increase of the surface tension. The spanning film then rotates further, as shown in Fig. 15b, and eventually detaches from the bubble [7]. This rotation is associated with a reduction in the length of the leading film, increasing the likelihood that the vertex will touch the channel wall and hence that the spanning film will leave the bubble behind. When the Gibbs-Marangoni parameter increases, the rate of surfactant redistribution is sufficient to equilibrate the surface tension around the vertex with other surface tensions elsewhere on that film, hence affecting the angle at which the films meet at the vertex and conferring stability on the foam. The critical (or maximum) driving velocity at which the system loses stability is shown in Fig. 16, confirming that the least stable systems are those with small (but not zero) values of G_M around one. Above this threshold, the larger the Gibbs-Marangoni parameter, the greater the maximum driving velocity.

Fig. 16 shows the effect of the lens bubble area on stability of the foam structure. The critical velocity for different bubble areas are plotted as a function of the Gibbs-Marangoni parameter. Larger bubbles are less stable, in the sense that they break down at a lower driving velocity, as observed previously when $G_M = 0$ [6,7]. This is a consequence of the total film length increasing with increasing bubble size, so that the resulting drag force on the bubble is greater overall. To alleviate the drag, the trailing film reorients to be closer to parallel with the channel walls over much of its length [7], therefore increasing the rotation angle of the spanning film and decreasing the length of the leading film, driving the onset of the instability of the structure [7].
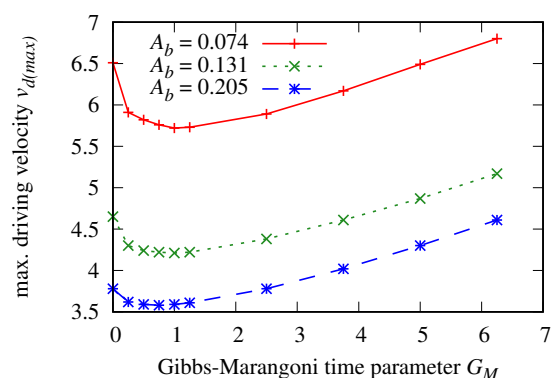
Figure 16: The effect of G_M on the maximum driving velocity $v_{d(max)}$ for different bubble areas. The size of the constriction is $\varepsilon = 0.3$ in all cases.
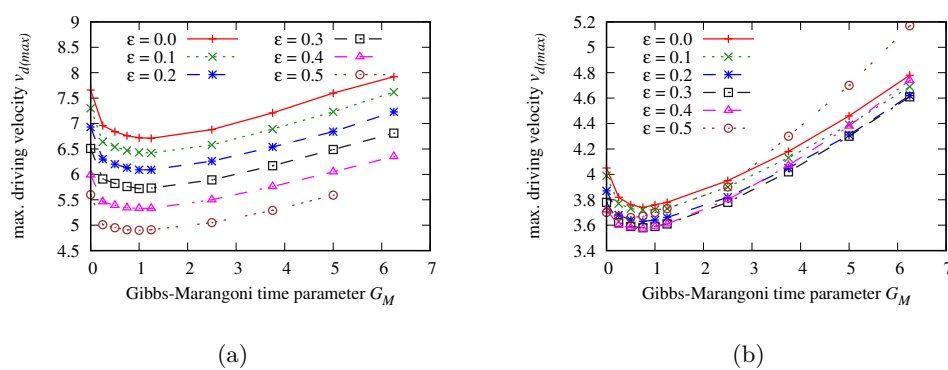

Figure 17: The effect of Gibbs-Marangoni parameter G_M on the maximum driving velocity $v_{d(max)}$ for various constriction widths and two bubble areas: (a) $A_b = 0.074$ and (b) $A_b = 0.205$.

The effect of constriction size on the stability is shown in Fig. 17, indicating that the maximum driving velocity (for two different bubble sizes) follows a similar trend to that seen in Fig. 16 with increasing influence of the Marangoni surfactant redistribution. For all values of ε, the critical velocity first decreases slightly with G_M and then increases strongly.

In general, the critical velocity decreases with increasing ε, towards the situation in which the channel is most constricted. This is consistent with what would happen for an abrupt change in channel width (see § 5(b)). An exception occurs in the case of a large bubble (with area $A_b = 0.205$) which, in the narrowest constriction ($\varepsilon = 0.5$) shows much greater stability at large values of G_M. At these large values of the Gibbs-Marangoni parameter and an arbitrarily chosen value of ε, the surface tension of the leading film decreases significantly as the film shrinks. In consequence there is a large discrepancy of surface tension between the leading film and the other two films. To compensate, the movement of the vertex stretches the leading film, delaying the instability (in a similar way to the delay of topological changes around a sheared vertex [24]). With very narrow constrictions however, the spanning film shrinks even further to respond to the channel geometry. As a result, it too has lower surface tension, leaving the trailing film with much higher surface tension to pull back on the vertex and prevent the topological transformation.

6. Conclusion

The viscous froth model for the calculation of film deformation in foam flow has been coupled with the Marangoni equation to simulate surfactant redistribution on a moving soap film. The Marangoni effect counters any gradients of surface tension that develop during flow, resulting in a narrower distribution of surfactant concentration along a film.

In the simple three-film foam structure examined here, surfactant redistribution opposes the shrinking of the leading film as the lens structure moves along a straight channel, and reduces the stretching of the spanning and trailing films, resulting in a taller bubble and enhancing foam stability. However, we identify an intermediate regime where the Gibbs elasticity is large enough to cause gradients of surface tension, but is not strong enough to redistribute the surfactant, resulting in an imbalance of tensions at the vertex, reducing the vertex height.

When the channel width varies, the range of driving velocities for which a stable structure can exist for a specified bubble size is reduced. The spanning film detaches from the lens and leaves the bubble behind, breaking up the foam.

The distribution of the surfactant occurs through tangential movement along the films, the velocity of which is determined by the Gibbs-Marangoni parameter and the gradient of surfactant surface concentration. This tangential movement can help to prevent a film from shrinking excessively, preventing topological changes in the foam structure. The films experience greater deformation when flowing through a constricted channel. The Marangoni surfactant redistribution reduces the deformation, again resulting in taller bubbles at a particular driving velocity. As a result, the lens structure is more stable with a larger Gibbs-Marangoni parameter. There is an intermediate regime where the Gibbs-Marangoni parameter is not sufficient to smooth out gradients of surface tension, reducing the range of possible driving velocities at which stable lens structures exist. Such a situation should be avoided in the use of foam as a displacement fluid, since it would lead to much of the pore space being filled with stationary lamellae stuck to walls and the only flowing foam would consist of single "bamboo" lamellae.

References

1. Drenckhan W, Cox SJ, Delaney G, Holste H, Kern N. 2005 Rheology of ordered foams - on the way to Discrete Microfluidics. *Colloids and Surfaces A: Physicochemical and Engineering Aspects* **263**, 52–64. 10.1016/j.colsurfa.2005.01.005.
2. Shadid N, Ceulen R, Nelemans P, Dirksen C, Veraart J, Schurink GW, Van Neer P, Vd Kley J, De Haan E, Sommer A. 2012 Randomized clinical trial of ultrasound-guided foam sclerotherapy versus surgery for the incompetent great saphenous vein. *British Journal of Surgery* **99**, 1062–1070. 10.1002/bjs.8781.
3. Jones SA, Dollet B, Slosse N, Jiang Y, Cox SJ, Graner F. 2011 Two-dimensional constriction flows of foams. *Colloids and Surfaces A: Physicochemical and Engineering Aspects* **382**,

18–23. 10.1016/j.colsurfa.2010.11.054.

4. Mamun CK, Rong JG, Kam SI, Liljestrand HM, Rossen WR. 2002 Extending foam technology from improved oil recovery to environmental remediation. In *Society of Petroleum Engineers Annual Technical Conference and Exhibition* pp. 1–13 San Antonio, Texas. 10.2118/77557-MS.

5. Géraud B, Jones SA, Cantat I, Dollet B, Méheust Y. 2016 The flow of a foam in a two-dimensional porous medium. *Water Resources Research* **52**, 773–790. 10.1002/2015WR017936.

6. Vitasari D, Cox S. 2017 A viscous froth model adapted to wet foams. *Colloids and Surfaces A: Physicochemical and Engineering Aspects* **534**, 8–15. 10.1016/j.colsurfa.2017.04.064.

7. Green TE, Bramley A, Lue L, Grassia P. 2006 Viscous froth lens. *Physical Review E* **74**, 051403. 10.1103/PhysRevE.74.051403.

8. Cox SJ, Weaire D, Mishuris G. 2009 The viscous froth model: steady states and the high-velocity limit. *Proceedings of the Royal Society A: Mathematical, Physical and Engineering Sciences* **465**, 2391–2405.

9. Kern N, Weaire D, Martin A, Hutzler S, Cox SJ. 2004 Two-dimensional viscous froth model for foam dynamics. *Physical Review E* **70**, 041411. 10.1103/PhysRevE.70.041411.

10. Weaire D, Hutzler S. 1999 *The Physics of Foams*. Oxford: Oxford University Press.

11. Embley B, Grassia P. 2011 Viscous froth simulations with surfactant mass transfer and Marangoni effects: Deviations from Plateau's rules. *Colloids and Surfaces A: Physicochemical and Engineering Aspects* **382**, 8–17. 10.1016/j.colsurfa.2011.01.013.

12. Cantat I, Cohen-Addad S, Elias F, Graner F, Hohler R, Pitois O, Rouyer F, Saint-Jalmes A. 2013 *Foams: Structure and Dynamics*. Oxford University Press.

13. Scriven LE, Sternling CV. 1960 The Marangoni effects. *Nature* **187**, 186–188. 10.1038/187186a0.

14. Vitasari D, Grassia P, Martin P. 2013 Surfactant transport onto a foam lamella. *Chemical Engineering Science* **102**, 405–423. /10.1016/j.ces.2013.08.041.

15. Zaccagnino F, Audebert A, Cox SJ. 2018 Simulation of surfactant transport during the rheological relaxation of two-dimensional dry foams. *Physical Review E* **98**, 022801. 10.1103/PhysRevE.98.022801.

16. Golemanov K, Denkov ND, Tcholakova S, Vethamuthu M, Lips A. 2008 Surfactant Mixtures for Control of Bubble Surface Mobility in Foam Studies. *Langmuir* **24**, 9956–9961. 10.1021/la8015386.

17. Green TE, Grassia P, Lue L, Embley B. 2009 Viscous froth model for a bubble staircase structure under rapid applied shear: An analysis of fast flowing foam. *Colloids and Surfaces A: Physicochemical and Engineering Aspects* **348**, 49–58. 10.1016/j.colsurfa.2009.06.028.

18. Durand M, Stone HA. 2006 Relaxation time of the topological T1 process in a two-dimensional foam. *Physical Review Letters* **97**, 226101. 10.1103/PhysRevLett.97.226101.

19. Dickinson E. 1999 Adsorbed protein layers at fluid interfaces: Interactions, structure and surface rheology. *Colloids and Surfaces B: Biointerfaces* **15**, 161–176. 10.1016/S0927-7765(99)00042-9.

20. Petit P, Seiwert J, Cantat I, Biance AL. 2015 On the generation of a foam film during a topological rearrangement. *Journal of Fluid Mechanics* **763**, 286–301. 10.1017/jfm.2014.662.

21. Raven JP, Marmottant P, Graner F. 2006 Dry microfoams: Formation and flow in a confined channel. *European Physical Journal B* **51**, 137–143. 10.1140/epjb/e2006-00197-6.

22. Marmottant P, Raven J. 2009 Microfluidics with foams. *Soft Matter* **5**, 3385–3388. 10.1039/b903276b.

23. Scriven LE, Sternling CV. 1964 On cellular convection driven by surface-tension gradients: Effects of mean surface tension and surface viscosity. *Journal of Fluid Mechanics* **19**, 321–340. 10.1017/S0022112064000751.

24. Grassia P, Embley B, Oguey C. 2012 A Princen hexagonal foam out of physicochemical equilibrium. *Journal of Rheology* **56**, 501–526. 10.1122/1.3687442.

25. Cantat I. 2011 Gibbs elasticity effect in foam shear flows: A non quasi-static 2D numerical simulation. *Soft Matter* **7**, 448–455. 10.1039/c0sm00657b.

26. Brakke KA. 1992 The Surface Evolver. *Experimental Mathematics* **1**, 141–165. 10.1080/10586458.1992.10504253.

27. Brakke KA. 1996 The Surface Evolver and the stability of liquid surfaces. *Philosophical Transactions: Mathematical, Physical and Engineering Sciences* **354**, 2143–2157. 10.1098/rsta.1996.0095.

28. Uteshev AY. 2014 Analytical solution for the generalized Fermat-Torricelli problem. *The American Mathematical Monthly* **121**, 318–331. 10.4169/amer.math.monthly.121.04.318.

29. Cantat I, Kern N, Delannay R. 2004 Dissipation in foam flowing through narrow channels. *EPL (Europhysics Letters)* **65**, 726–732. 10.1209/epl/i2003-10169-0.

30. Cantat I, Delannay R. 2005 Dissipative flows of 2D foams. *European Physical Journal E* **18**, 55–67. 10.1140/epje/i2004-10154-5.

31. Grassia P, Mas-Hernãndez E, Shokri N, Cox SJ, Mishuris G, Rossen WR. 2014 Analysis of a model for foam improved oil recovery. *Journal of Fluid Mechanics* **751**, 346–405. 10.1017/jfm.2014.287.

32. Grassia P, Lue L, Torres-Ulloa C, Berres S. 2017 Foam front advance during improved oil recovery: Similarity solutions at early times near the top of the front. *Journal of Fluid Mechanics* **828**, 527–572. 10.1017/jfm.2017.541.

33. Satomi R, Grassia P, Oguey C. 2013 Modelling relaxation following T1 transformations of foams incorporating surfactant mass transfer by the Marangoni effect. *Colloids and Surfaces A: Physicochemical and Engineering Aspects* **438**, 77–84. 10.1016/j.colsurfa.2012.11.075.

34. Grassia P, Oguey C, Satomi R. 2012 Relaxation of the topological T1 process in a two-dimensional foam. *European Physical Journal E* **35**, 64. 10.1140/epje/i2012-12064-3.